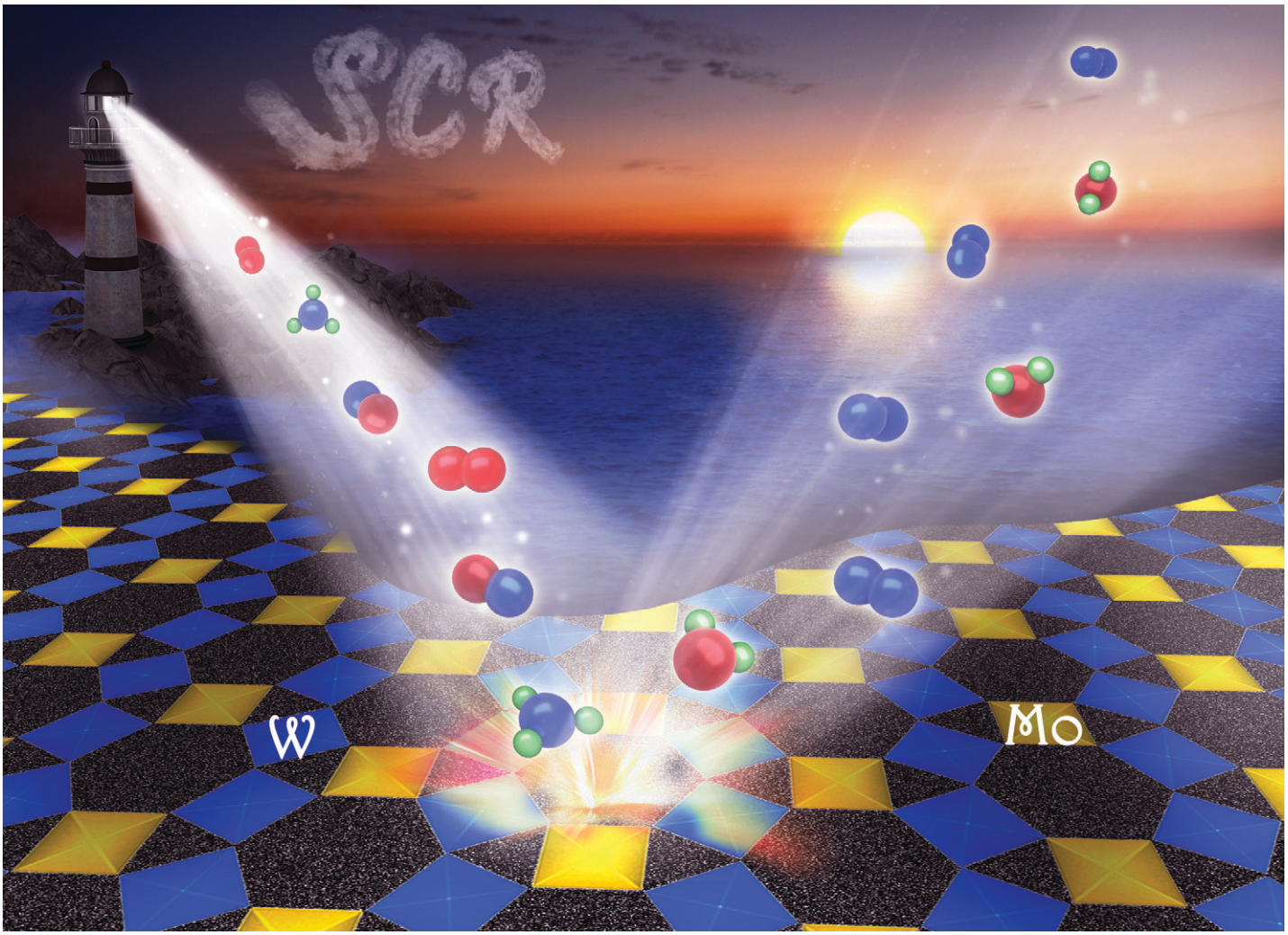


**Showcasing research from Xingfu Tang's Laboratory, Department of Environmental Science and Engineering, Fudan University, Shanghai, China.**

Tuning electronic states of catalytic sites enhances SCR activity of hexagonal $WO_3$ by Mo framework substitution

Catalytic sites of selective catalytic reduction (SCR) of NO with $NH_3$ are identified to be located at the tunnel openings of the Mo-doped hexagonal $WO_3$ catalyst. The framework substitution by Mo reduces the bandgap between the highest occupied molecular orbitals and the lowest unoccupied molecular orbitals, thus accelerating electron transfer in SCR redox cycles and enhancing catalytic activity.

## As featured in:


See Xingfu Tang *et al.*, *Catal. Sci. Technol.*, 2017, **7**, 2467.

ROYAL SOCIETY OF CHEMISTRY

rsc.li/catalysis

Registered charity number: 207890

Catalysis Science & Technology

PAPER

View Article Online
View Journal | View Issue

Check for updates

Cite this: *Catal. Sci. Technol.*, 2017, 7, 2467

# Tuning electronic states of catalytic sites enhances SCR activity of hexagonal $WO_3$ by Mo framework substitution†

Yaxin Chen,‡[a] Zichenxi Dong,‡[a] Zhiwei Huang,[a] Meijuan Zhou,[a] Jiayi Gao,[a] Junxiao Chen,[a] Chao Li,[a] Zhen Ma,[a] Jianmin Chen[a] and Xingfu Tang *[ab]

Received 4th March 2017,
Accepted 25th April 2017

DOI: 10.1039/c7cy00416h

rsc.li/catalysis

Selective catalytic reduction (SCR) of NO with $NH_3$ essentially proceeds *via* redox cycles, in which electrons transfer between reactants and catalytically active sites (CASs). Hence, the electronic states of CASs play a crucial role in determining the SCR activity of catalysts. Herein, we tune the electronic structures of CASs *via* substitution of the hexagonal $WO_3$ framework by Mo (Mo–HWO). The resulting Mo–HWO catalyst shows a high NO conversion of 80% at 350 °C at a gas hourly space velocity of 32 000 $h^{-1}$, in the presence of high-concentration $SO_2$ (2700 mg $m^{-3}$) and 10 vol% $H_2O$. Various characterization results demonstrate that the CASs responsible for $NH_3$ adsorption and activation are located at the tunnel openings, *i.e.*, the (001) top-facets of Mo–HWO nanorods. The framework substitution by Mo reduces the bandgap between the highest occupied molecular orbitals and the lowest unoccupied molecular orbitals by hybridizing W and Mo cations with their bridging oxygen ions, thus making the electron transfers in SCR redox cycles relatively easy and leading to improved catalytic activity. This work could assist the rational design of catalysts by tuning the electronic states of CASs.

Published on 25 April 2017. Downloaded by Fudan University on 11/28/2018 6:17:42 AM.

## 1. Introduction

Nitrogen oxides ($NO_x$), as typical atmospheric pollutants, have a great contribution to acid rain, photochemical smog, and ozone formation,[1] and hence have attracted great attention in the past several decades. Selective catalytic reduction (SCR) of $NO_x$ with $NH_3$ for controlling $NO_x$ emissions from stationary sources and mobile sources is a promising technology.[2,3] $V_2O_5$–$WO_3(MoO_3)$/$TiO_2$ catalysts have been commercially used for SCR because of their high catalytic activity and strong $SO_2$ tolerance.[2–4] However, the toxicity of vanadium demands that $V_2O_5$–$WO_3(MoO_3)$/$TiO_2$ catalysts should be replaced by environmentally friendly catalysts in the long run. SCR essentially follows a reduction–oxidation mechanism, and thus the activity is intimately associated with the redox properties of catalysts.[5,6] $MnO_2$-based catalysts with good redox properties show high catalytic activity in SCR, especially at low temperatures,[7–9] but their poor sulfur tolerance makes it impossible for them to be used under practical SCR conditions.[9] Thus, it is highly desirable to develop environmentally benign and sulfur-tolerant SCR catalysts for practical applications.

Although $WO_3$ and $MoO_3$ in $V_2O_5$–$WO_3(MoO_3)$/$TiO_2$ can promote the SCR activity,[10,11] stabilize the $TiO_2$ structure,[12,13] and inhibit the oxidation of $SO_2$, they often serve as promoters in SCR because their redox ability is much weaker than that of $V_2O_5$.[2,3] An appealing alternative is to improve the redox ability of $WO_3$ and $MoO_3$, so they can act as active phases. In fact, $WO_3$ and $MoO_3$ have been used as active components of SCR catalysts after their redox properties are improved.[14,15] For instance, Kobayashi *et al.* found that $WO_3$/$TiO_2$ prepared by coprecipitation is more active, in the presence of 10% $H_2O$, than $WO_3$/$TiO_2$ prepared by conventional impregnation due to the enhanced redox ability of $WO_3$ in the former catalyst.[14] Giamello *et al.* found that surface $Mo^{5+}$ centers are responsible for SCR *via* a $Mo^{6+}$/$Mo^{5+}$ redox cycle resulting from the interaction between the $MoO_3$ phase and the $TiO_2$ support.[15] Thus, it is feasible for $WO_3$ and $MoO_3$ to become active phases by improving their redox ability.

$WO_3$ has different crystalline structures, including hexagonal and monoclinic phases. Hexagonal $WO_3$ (HWO), with a space group of *P6/mmm*, is constructed from corner-sharing $WO_6$ octahedra.[16] HWO has strong acidity and excellent reducibility due to the co-existence of $W^{6+}$ and $W^{5+}$, and thus it can be used as an active component of catalysts.[17] Because

[a] *Shanghai Key Laboratory of Atmospheric Particle Pollution & Prevention (LAP³), Department of Environmental Science & Engineering, Institute of Atmospheric Sciences, Fudan University, Shanghai 200433, China.*
*E-mail: tangxf@fudan.edu.cn*
[b] *Jiangsu Collaborative Innovation Center of Atmospheric Environment and Equipment Technology (CICAEET), Nanjing University of Information Science & Technology, Nanjing, 210044, China*

† Electronic supplementary information (ESI) available. See DOI: 10.1039/c7cy00416h

‡ These authors contributed equally to this work.

Published on 25 April 2017. Downloaded by Fudan University on 11/28/2018 6:17:42 AM.

the electronic structures and the ionic sizes of Mo and W are similar, the hexagonal bronze structure can be maintained if $WO_6$ in the HWO framework is substituted by $MoO_6$ (*i.e.*, to form Mo–HWO).[18–22] After such framework substitution, the redox properties of HWO may be tuned. It was reported that the partial substitution of W in HWO by Mo can improve the sensing properties towards $NH_3$ or $NO_x$, which are closely associated with the redox properties of Mo–HWO.[21,22] The standard reduction potential ($\varphi^{\ominus}$) of $Mo^{6+/5+}$ is ~0.40 V, close to that of $W^{6+/4+}$ ($\varphi^{\ominus}$ = ~0.39 V),[23,24] and hence the reaction between Mo and W cations is favorable in Mo–HWO.[25] The Zener exchange may enhance the redox ability of Mo–HWO, *i.e.*, the substitution of W in HWO by Mo improves the ability to activate lattice oxygen and gaseous oxygen. It is well known that the activation of $NH_3$ or $NO_x$ and oxygen plays crucial roles in SCR, which motivates us to investigate SCR over Mo–HWO.

Herein, we investigate the SCR performance of Mo–HWO. Firstly, we synthesize Mo–HWO by a hydrothermal method, test its catalytic activity in SCR, and determine the structure of Mo–HWO by synchrotron X-ray diffraction (SXRD) and transmission electron microscopy (TEM). Next, the catalytically active sites (CASs) of Mo–HWO are identified by SXRD, $^1$H magic angle spinning nuclear magnetic resonance ($^1$H MAS NMR), and hydrogen temperature-programmed reduction ($H_2$-TPR). Finally, X-ray absorption near-edge structure (XANES) and X-ray photoelectron spectra (XPS) coupled with theoretical calculations are used to illustrate why the substituted Mo can dramatically enhance the SCR performance of HWO.

# 2. Experimental

## 2.1 Catalyst synthesis

Mo–HWO powders were synthesized *via* a hydrothermal method. Ammonium paratungstate [$(NH_4)_6W_{12}O_{39}{\cdot}xH_2O$, 1.300 g], ammonium sulfate [$(NH_4)_2SO_4$, 8.600 g], ammonium molybdate [$(NH_4)_6Mo_7O_{24}$, 0.940 g], and oxalic acid ($H_2C_2O_4$, 2.100 g) were dissolved in deionized $H_2O$ (60 mL).[16] The resulting solution was transferred to a 100 mL autoclave and kept at 180 °C in an oven for 18 h. The final slurry was filtered, washed with deionized $H_2O$, and dried at 80 °C. The resulting solid was calcined at 350 °C for 4 h in air to give the Mo–HWO catalyst. HWO powders were prepared using the same method as Mo–HWO without the addition of $(NH_4)_6Mo_7O_{24}$ during the preparation process. To further load $K^+$, Mo–HWO was impregnated with a $K_2SO_4$ solution. K/Mo–HWO was obtained after being dried at 105 °C for 12 h and then calcined at 350 °C for 12 h. The $K^+$ loading was set to be 400 μmol $g_{cat}^{-1}$.

## 2.2 Catalytic evaluation

SCR reactions were conducted in a fixed-bed quartz reactor (i.d. = 8 mm) under atmospheric pressure. A certain amount of catalyst (40–60 mesh) was charged for each run. For the activity tests, the feed gas was composed of 500 ppm NO, 500 ppm $NH_3$ and 3.0 vol% $O_2$, and balanced using $N_2$. The gas hourly space velocity (GHSV) was fixed at 192 000 $h^{-1}$. The gas flow rate was 1000 mL $min^{-1}$, and the amount of the catalyst was 0.5 g. For the water- and $SO_2$-resistance tests, the feed gas was composed of 1000 ppm NO, 1000 ppm $NH_3$, 3.0 vol% $O_2$, 2700 mg $m^{-3}$ $SO_2$ and 10 vol% $H_2O$ vapor, and balanced using $N_2$. The GHSV was fixed at 32 000 $h^{-1}$. The gas flow rate was 500 mL $min^{-1}$, and the amount of the catalyst was 1.5 g. The concentrations of NO and $NO_2$ in the inlet and outlet gas were measured using an on-line chemiluminescence NO–$NO_2$–$NO_x$ analyzer (42i-HL, Thermo Electron Corporation, USA). The data were recorded after the reactions reached a steady state. The conversion rate ($X_{NO}$) was defined as follows: $X_{NO}\% = (1 - [NO]_{out}/[NO]_{in}) \times 100\%$, where $[NO]_{out}$ and $[NO]_{in}$ represent the NO concentrations of the inlet and outlet gas, respectively. Arrhenius plots were obtained according to the SCR activity of the samples at 260–320 °C with $X_{NO}\%$ less than 20%. We eliminated the effects from the external and internal diffusion by varying the linear velocity of the feed gas passing through the catalysts and the size of catalysts' particles, respectively, for the reaction kinetics, as shown in Fig. S1 (ESI†).

## 2.3 Catalyst characterization

SXRD patterns were recorded at BL14B of the Shanghai Synchrotron Radiation Facility (SSRF) at a wavelength of 0.6883 Å. Rietveld refinement analyses of the diffraction profiles were conducted using the Rietica v1.77 program. TEM, high-resolution TEM (HRTEM), and scanning TEM energy dispersive X-ray spectroscopy (STEM-EDX) mapping were conducted on a JEM 2100F transmission electron microscope. XPS experiments were carried out with an RBD 147 upgraded PerkinElmer PHI 5000C ESCA system equipped with a hemispherical electron energy analyzer. The Mg Kα ($\lambda$ = 1253.6 eV) anode was operated at 14 kV and 20 mA. The spectra were recorded in constant pass energy mode with a value of 46.95 eV. The experimental errors were within ±0.2 eV. Data analysis and processing were undertaken using the XPSPeak4.1 software with the Shirley type background. $H_2$-TPR experiments were performed using a Micromeritics 2920 adsorption instrument with a thermal conductivity detector to monitor the consumed $H_2$. $H_2$-TPR was conducted at 10 °C $min^{-1}$ under a 50 mL $min^{-1}$ flow of 5 vol% $H_2$ in Ar.

$^1$H MAS NMR spectra were recorded on a Bruker AVANCE III 400 WB spectrometer. The chemical shifts of $^1$H were referenced to TMS at 0 ppm. $^1$H MAS NMR experiments were performed at a spinning rate of 20 kHz. $^1$H MAS spectra were recorded in a spin echo pulse sequence ($\pi/2$–$\tau$–$\pi$–$\tau$-acquire), where $\tau$ is equal to one rotor period (rotor synchronized). The excitation pulse length was 2.3 μs ($\pi/2$), and typically ~40 scans were accumulated with a 5 s delay. XANES spectra were measured at the W $L_3$-edge at BL14W of the SSRF with an electron beam energy of 3.5 GeV and a ring current of 200–300 mA. Data were collected with a fixed exit monochromator using two flat Si(311) crystals. The XANES spectra were

 This journal is © The Royal Society of Chemistry 2017

Published on 25 April 2017. Downloaded by Fudan University on 11/28/2018 6:17:42 AM.

acquired at an energy step of 0.5 eV. The raw data were analyzed using the IFEFFIT 1.2.11 software package. Raman spectra were obtained using a Horiba Jobin Yvon XploRA spectrometer. The measurements with an excitation laser of 532 nm were calibrated with the Raman peak of Si at 520 $cm^{-1}$. The interchangeable holographic grating of the spectrometer is 1800 grooves per mm. The laser powers are less than 1 mW to avoid overheating of the samples.

### 2.4 Theoretical calculations

Density functional theory (DFT) calculations were performed with the Vienna *ab initio* Simulation Package (VASP).[26,27] The exchange and correlation effects are described by the general gradient approximation (GGA) method.[28] The projector-augmented wave (PAW) method describes the interactions between the core and valence electrons. The plane-wave energy cutoff was set at 450 eV. The Perdew–Burke–Ernzerhof (PBE) exchange-correlation functional method was used in our calculations.[29] The lattice constant for a conventional hexagonal cell with a space group of *P6/mmm* is 7.319 Å × 7.319 Å × 3.881 Å. A super cell of 12 formula units of HWO was employed in the charge calculations. The (001) surface of Mo–HWO was cut from the stable supercell after the geometry was optimized.

## 3. Results and discussion

### 3.1 Catalytic activity and catalyst structures

As shown in Fig. 1a, the activity of HWO is significantly low under the SCR conditions (GHSV = 192 000 $h^{-1}$, in the absence of $SO_2$ and $H_2O$). The NO conversion ($X_{NO}$) on HWO is lower than 40% even at 350 °C. However, the $X_{NO}$ on Mo–HWO is much higher. The $X_{NO}$ reaches ~75% at a high GHSV of 192 000 $h^{-1}$ at 350 °C. In the chemical kinetic regime where the $X_{NO}$ is lower than 15%, the $X_{NO}$ of Mo–HWO (12%) is four times as that of HWO (3%) at 250 °C. Furthermore, we tested the stability of Mo–HWO and HWO under mimicked working conditions (2700 mg $m^{-3}$ $SO_2$, 10 vol% $H_2O$, GHSV 32 000 $h^{-1}$). Mo–HWO shows higher activity and stability than HWO in the presence of high-concentration $SO_2$ and $H_2O$ in the feed gas, as shown in the stability test in Fig. 1a and Fig. S2 (ESI†).

The crystal structures of HWO and Mo–HWO were studied using SXRD. As shown in Fig. 1b, all the diffraction peaks can be indexed to the hexagonal tungsten bronze structure with a space group of *P6/mmm* (JCPDS 33-1387).[16] HWO has one-dimensional tunnels where different cations can insert themselves. Moreover, the framework W ions of HWO can exist as $W^{6+}$, $W^{5+}$, and $W^{4+}$ with different oxidation states and ionic radii.[30] These framework W ions can be readily substituted by Mo,[18–22] V,[31] and Nb.[32] The SXRD pattern of Mo–HWO is also shown in Fig. 1b. The hexagonal tungsten bronze structure is preserved after the incorporation of Mo in HWO, and no $MoO_x$ species appear. However, the structure of HWO is modified, as judged from the intensity of the peaks after the introduction of Mo. The intensity ratio of the

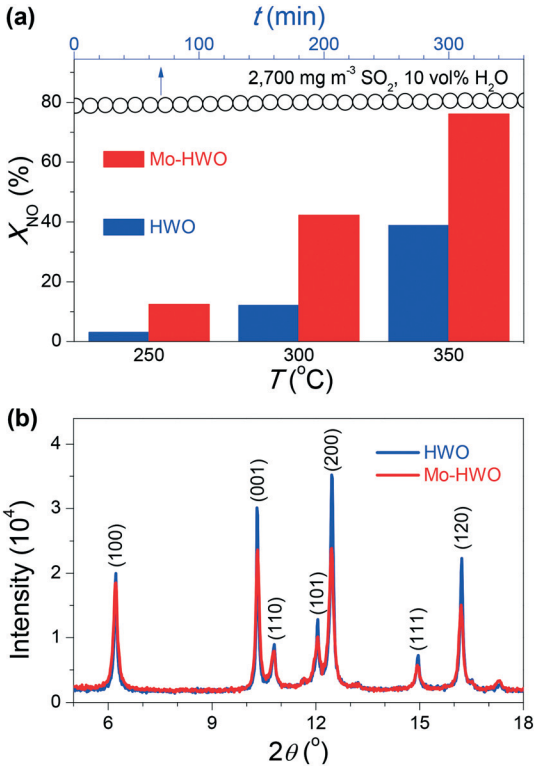


**Fig. 1** (a) The $X_{NO}$ of HWO and Mo–HWO at different reaction temperatures (*T*), and the $X_{NO}$ as a function of time (*t*) on stream over Mo–HWO at 350 °C in the presence of 2700 mg $m^{-3}$ $SO_2$ and 10 vol% $H_2O$. (b) SXRD patterns of HWO and Mo–HWO.

(001) plane to the (100) plane is ~1.4 for HWO, whereas it decreases to ~1.2 for Mo–HWO, indicating that the incorporation of Mo suppressed the growth of HWO along the [001] direction. Similarly, the intensity ratio of the HWO(200) plane to the HWO(100) plane is ~1.6 for HWO, whereas it decreases to 1.2 for Mo–HWO, indicating the lattice distortion of the HWO structure after the incorporation of Mo. Because Mo ions have almost the same ionic radius as W ions, for instance, the radius of $Mo^{5+}$ (0.75 Å) is the same as that of $W^{6+}$ (0.74 Å),[33] no distinct shift in the diffraction peaks of HWO is observed after the incorporation of Mo.[34] The results support the substitution of the HWO framework by Mo.

The effect of the Mo framework substitution on the morphologies and structures of HWO was studied by TEM, HRTEM, and STEM (Fig. 2). HWO has a rod-shaped morphology with a mean width of ~80 nm and a mean length of ~370 nm (Fig. 2a, S3 and S4, ESI†). The fringe of 3.8 Å, assigned to the HWO(001) spacing, can be clearly observed by HRTEM (Fig. 2b), implying that HWO rods grow along the [001] axis because the (001) plane has a higher surface energy than other low-index Mille planes such as the (100) plane.[35] The growth direction of HWO is also in agreement with a geometrical prediction made by the Bravais–Friedel Donnay–Harker method,[36] as well as some experimental observations.[37] After the Mo framework substitution shown in Fig. 2c–f, Mo–HWO still preserves the rod-shaped structure

Published on 25 April 2017. Downloaded by Fudan University on 11/28/2018 6:17:42 AM.

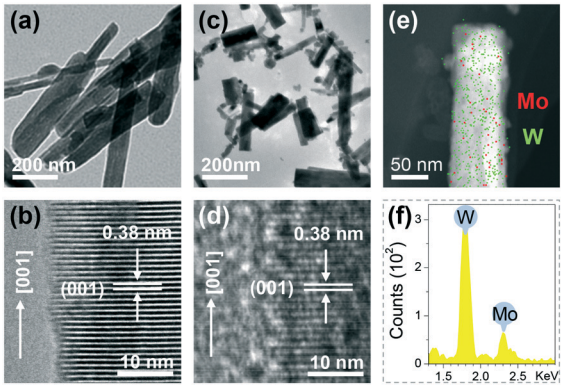


Fig. 2 TEM (a and c) and HRTEM images (b and d) of HWO (a and b) and Mo–HWO (c and d). STEM image and EDX mapping image (e), and EDX spectrum (f) of Mo–HWO.

in the [001] growth direction, but the length (~260 nm) decreases more distinctly than the width (~60 nm) (Fig. S3 and S4, ESI†) in comparison with HWO, implying that the aspect ratio decreases. Hence, the framework substitution by Mo increases the fraction of the (001) planes exposed. Moreover, the relatively obscure fringe of the (001) plane in the HRTEM image (Fig. 2d) and the highly dispersed Mo species (Fig. 2e) further demonstrate the Mo framework substitution, as evidenced by the SXRD patterns (Fig. 1b) and Raman spectra (Fig. S5, ESI†).

### 3.2 Identification of catalytically active sites

As discussed above, the (001) top-facets of Mo–HWO, consisting of the tunnel openings, have higher surface energy than the (100) side-facets,[35] and hence the CASs may be located at the (001) facets of Mo–HWO. To verify this hypothesis, we anchored $K^+$ ions (a SCR catalyst poison) onto the tunnel openings. Fig. 3a shows the SXRD pattern with Rietveld refinement of Mo–HWO after loading $K^+$ (K/Mo–HWO), and the crystallographic data and structure parameters obtained by the Rietveld refinement are listed in Tables S1 and S2,† respectively. Obviously, $K^+$ ions are situated at the Wyckoff 1*a* sites or at the crystallographic (0,0,0) sites.[16,38] According to our recent report,[38] $K^+$ ions occupy the tunnel openings of the (001) top-facets. After the addition of $K^+$, the catalytic activity of Mo–HWO decreases drastically (Fig. S6, ESI†), demonstrating that the tunnel openings should be the CASs for SCR. Moreover, the tunnel openings on the (001) facets are suitable for $NH_3$ adsorption and subsequent activation.[36,39]

$NH_3$ adsorption and activation are commonly regarded as important steps for SCR. We studied $NH_3$ adsorption on Mo–HWO surfaces by using $^1H$ MAS NMR spectroscopy. As shown in Fig. 3b, before the adsorption of $NH_3$, a strong symmetric peak shows up at a chemical shift ($\delta$) of ~6.8 ppm. This peak can be assigned to the hydrogen resonance of the lattice $NH_4^+$ in the Mo–HWO tunnels. Here, we denote it as $NH_4^+$ at a "static state" because $NH_4^+$ ions are strictly confined in the

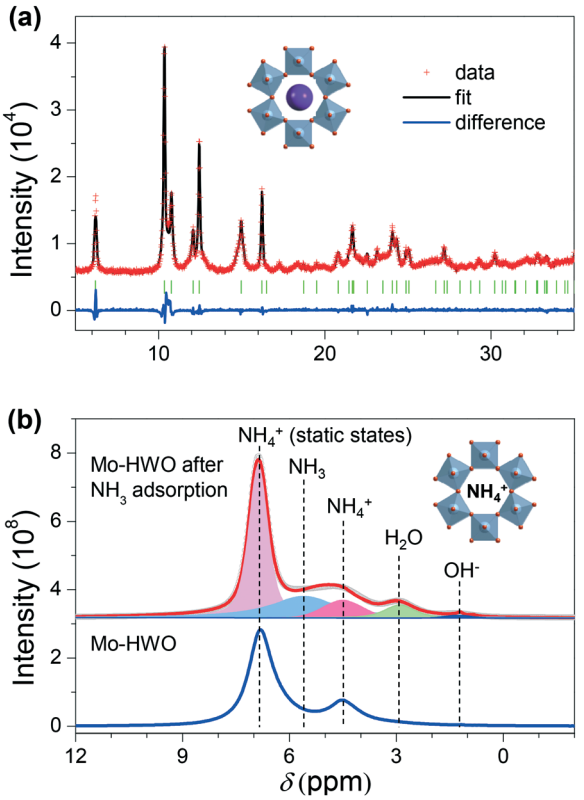


Fig. 3 (a) SXRD pattern with Rietveld refinement of K/Mo–HWO, together with the differential pattern. The peak positions of all possible Bragg reflections are marked with short green vertical lines. The purple ball represents the $K^+$ ion. (b) $^1H$ MAS NMR spectra of Mo–HWO before and after $NH_3$ adsorption at 110 °C in $N_2$.

tunnel lattice sites of Mo–HWO.[39,40] Another relatively weak peak at ~4.8 ppm is assigned to the hydrogen resonance of $NH_4^+$ adsorbed in the tunnels.[40] This $NH_4^+$ species might have a relatively weak interaction with the Mo–HWO tunnels.[41] No resonant peaks due to $H_2O$ can be observed because Mo–HWO was annealed at 350 °C.

After the adsorption of $NH_3$ on Mo–HWO in an inert $N_2$ gas flow, two new resonant features appear at chemical shifts of ~1.2 and ~2.8 ppm (Fig. 3b), assigned to the $OH^-$ groups and $H_2O$, respectively.[40] The data indicate that $NH_3$ is oxidized by the lattice oxygen of Mo–HWO. The intensity of the peak due to the lattice $NH_4^+$ at a chemical shift of 6.8 ppm increases, possibly originating from the reaction of the produced $H_2O$ with adsorbed $NH_3$ ($NH_3 + H_2O \rightarrow NH_4^+ + OH^-$), further indicating that $NH_3$ can be activated by Mo–HWO. The occurrence of this activation process is possibly associated with the tunnel structures, because the amount of $NH_3$ adsorbed on monoclinic $WO_3$ without any tunnel is significantly less than the amount of that adsorbed on HWO with the tunnel structure.[39] Moreover, according to the curve-fitting of the $^1H$ NMR spectrum of Mo–HWO, the chemical shift at ~5.6 ppm can be ascribed to $NH_3$.[40] Often, SCR does not occur in the HWO tunnels due to the big molecular sizes of the reactant $O_2$ and the produced $N_2$. Thus, SCR mainly occurs at the tunnel openings.

 This journal is © The Royal Society of Chemistry 2017

Published on 25 April 2017. Downloaded by Fudan University on 11/28/2018 6:17:42 AM.

$H_2$-TPR experiments were conducted to further identify the CASs. The reduction of the bulk lattice oxygen species of pure $WO_3$ often occurs at temperatures higher than ~570 °C,[42] and thus possible $H_2$ consumption at temperatures below ~570 °C should be assigned to the surface lattice oxygen species. Fig. S7 (ESI†) shows the $H_2$-TPR profiles of HWO, Mo–HWO, and K/Mo–HWO at 250–900 °C. A reduction peak at ~750 °C with an onset reduction temperature of ~600 °C can be ascribed to the reduction of the bulk lattice oxygen of HWO to form $WO_2$.[43] After the Mo framework substitution, this bulk reduction peak shifts to ~640 °C for Mo–HWO and the onset temperature is ~550 °C, while the reduction feature of this peak almost remains unchanged after the $K^+$ loading. Thus, the weak reduction peaks at temperatures lower than ~550 °C can be due to the reduction of the surface lattice oxygen.

The reduction of the surface lattice oxygen species of the samples is shown in the $H_2$-TPR profiles in Fig. 4. Similar reduction features for these three samples are observed. These features can be fitted into two reduction peaks, *i.e.*, the low-temperature (LT) and high-temperature (HT) peaks. The LT and HT peaks can be assigned to the reduction of the high surface energy (001) top-facets and the relatively low surface energy (100) side-facets, respectively, because these three samples expose only two kinds of facets on the surfaces.[16] The LT peaks of these three samples are almost located at the same reduction temperature of ~400 °C, while the calculated amounts of consumed $H_2$ are distinctly different from each other. The Mo framework substitution leads to a considerable increase of the $H_2$ consumption based on the LT peaks, in line with the increasing fraction of the (001) top-facets due to the higher aspect ratio of Mo–HWO to HWO. Note that the amount of $H_2$ consumption determined from the LT peak of Mo–HWO dramatically decreases from ~780 to ~110 μmol $g_{cat}^{-1}$ after $K^+$ ions occupied the tunnel openings on the (001) facets. Hence, the tunnel openings of Mo–HWO are the CASs. When $K^+$ ions occupy the CASs, the redox ability of the CASs drastically decreases, leading to much lower SCR activity (Fig. S6, ESI†).

Both the amount of the $H_2$ consumption and the reduction temperature of the HT peak of Mo–HWO (due to the reduction of the surface lattice oxygen on the (100) side-facets) remain almost unchanged after $K^+$ ions occupy the (001) top-facets. This further demonstrates that the CASs are not situated on the (100) facets, but located only on the (001) facets. Note that the onset of the reduction of Mo–HWO occurs at a much lower temperature than that of HWO, allowing Mo–HWO to exhibit an activation energy (~37 kJ $mol^{-1}$) much lower than that of HWO (~67 kJ $mol^{-1}$) in SCR at low reaction temperature (Fig. S8, ESI†). Thus, the Mo framework substitution not only increases the number of CASs but also enhances the redox ability of the CASs.

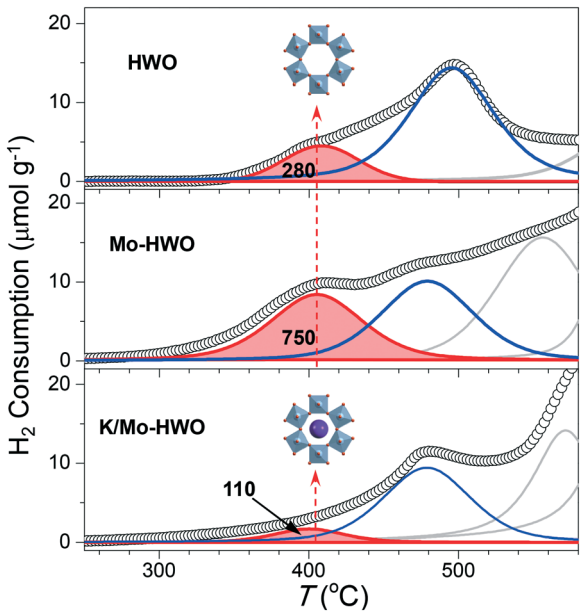


**Fig. 4** $H_2$-TPR profiles of HWO, Mo–HWO and K/Mo–HWO. The red shades show the reduction of the (001) top-facets, and the numbers in the shades are the corresponding amounts of the $H_2$ consumption during the reduction process. The purple ball represents the $K^+$ ion.

### 3.3 Electronic states of catalytically active sites

Both the catalytic activity and the redox ability are intimately associated with the electronic states of the CASs.[44] Thus, the effect of the Mo framework substitution on the electronic structures of W was investigated by using XANES and XPS. Fig. 5 shows the W XANES spectra and the corresponding second-derivative spectra of HWO and Mo–HWO at the W $L_3$-edge. Two overlapping absorption peaks attributed to the $2p_{3/2} \rightarrow e_g$ and $2p_{3/2} \rightarrow t_{2g}$ transitions appear in the XANES spectrum of HWO. These peaks shift to the low absorption energies after Mo substitution, indicating that the lowest unoccupied orbitals of W decrease in energy. The crystal field splitting energy (10*Dq*) of HWO is calculated to be ~4.5 eV according to the second-derivative spectra, and it decreases to 4.2 eV after the Mo framework substitution, indicating the decrease of the oxidation states of W.[45]

The oxidation states of Mo–HWO surfaces were studied by XPS (Fig. 5b). The $W^{6+}$ and $W^{5+}$ species with a ratio of 5 : 1

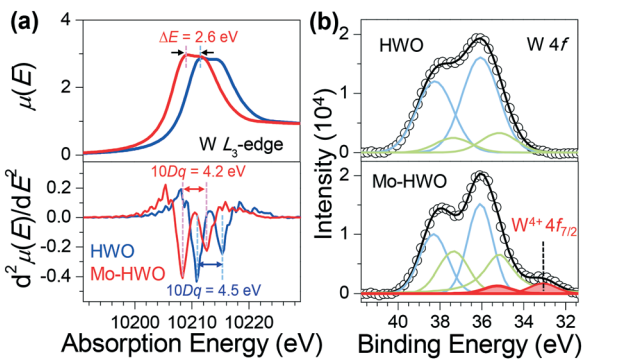


**Fig. 5** (a) W $L_3$-edge XANES and the corresponding second-derivative spectra of HWO and Mo–HWO. (b) W 4f XPS of HWO and Mo–HWO.

Published on 25 April 2017. Downloaded by Fudan University on 11/28/2018 6:17:42 AM.

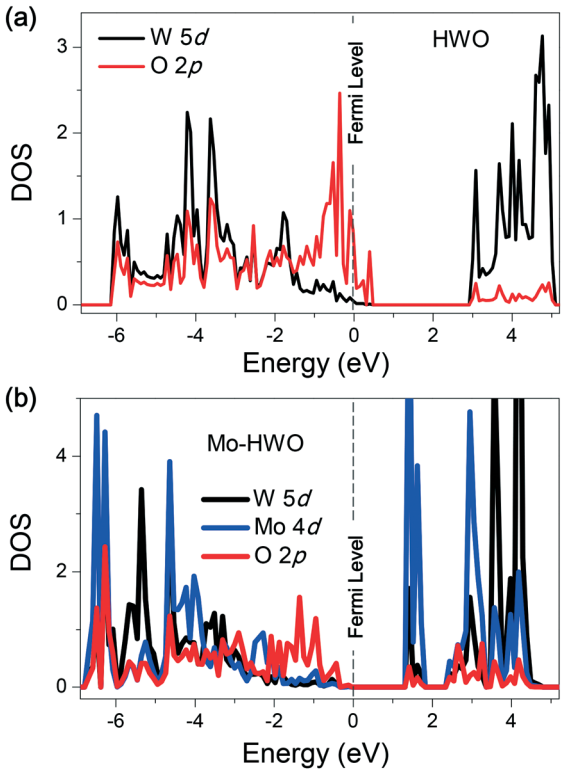


**Fig. 6** (a) Projected O and W DOS of the (001) facet of HWO. (b) Projected O, W and Mo DOS of the (001) facet of Mo–HWO.

are present in HWO, which is consistent with the hexagonal tungsten oxide with a formula of $AW^{6+}{}_5W^{5+}O_{18}$, where A represents $H^+$ and/or $NH_4^+$ in the tunnels for charge balance.[39] After the Mo framework substitution, the average oxidation states of W slightly decrease, in line with the decrease of the 10*Dq* value obtained from the XANES spectra at the W $L_3$-edge (Fig. 5a). Note that an extra XPS peak appears at a low binding energy of ~33.1 eV. After curve-fitting, the peak can be assigned to the $W^{4+}$ $4f_{7/2}$ XPS line.[39] Consequently, the W species in Mo–HWO include $W^{6+}$, $W^{5+}$, and $W^{4+}$ (see Table S3† for more details), *i.e.*, the electronic states of W in Mo–HWO are tuned by the Mo framework substitution.

The co-presence of $W^{6+}$, $W^{5+}$, and $W^{4+}$ may be important for improving the SCR activity. Similar standard reduction potentials, such as ($\varphi^{\ominus}$), $\varphi^{\ominus}$ ($W^{6+}/W^{5+}$) = −0.03 V and $\varphi^{\ominus}$ ($W^{5+}/W^{4+}$) = −0.04 V,[23] allow W to transfer between different oxidation states, thus enhancing the redox ability, as evidenced by the LT onset of the $H_2$-TPR profile of Mo–HWO (Fig. 4). Meanwhile, $Mo^{6+}$ and $Mo^{5+}$ co-exist in Mo–HWO as shown in the Mo 3d XPS in Fig. S9 and Table S3.† Likewise, similar $\varphi^{\ominus}$ values of $Mo^{6+}/Mo^{5+}$ (0.40 V)[23] and $W^{6+}/W^{4+}$ (0.39 V)[24] might make the reaction ($W^{6+}$ + $2Mo^{5+}$ = $W^{4+}$ + $2Mo^{6+}$) occur more easily, thus accelerating the electron transfer *via* the Mo–O–W bridge in Mo–HWO. Although the reduction potentials are obtained in aqueous solution, Owen *et al.* suggested that the reduction potentials of many cations in the solid states also follow a similar sequence.[46]

To shed light on the electronic states of the CASs of Mo–HWO, the projected density of states (DOS) of HWO and Mo–HWO are calculated by DFT (Fig. 6). For HWO, the DOS of O 2p and W 5d appear in the same energy regimes, implying the presence of W–O hybridization. Thus, the bandgap between the highest occupied molecular orbital (HOMO) and the lowest unoccupied molecular orbital (LUMO) is ~2.5 eV. The bandgap is then reduced to ~1.2 eV after the Mo framework substitution mainly caused by a downshift in energy of the LUMO, which is consistent with the experimental data that the absorption edge shifts to the low energy region after the incorporation of Mo (Fig. 5a). Likewise, the hybridization between the W and Mo cations through interactions with the bridging O atoms implicitly occurs because the DOS of W, Mo, and O in Mo–HWO are almost in the same energy regimes. Thus, owing to the Mo–O–W hybridization and the narrow bandgap between HOMO–LUMO, the electron transfer between the W and Mo *via* the bridging O is expected to become relatively easy,[47] leading to the co-existence of several oxidation states of W and Mo. In all, the Mo framework substitution reduces the bandgap between the HOMO and LUMO and increases the redox ability of the CASs, thus being favorable for SCR.

## 4. Conclusions

In conclusion, we tuned the electronic states of the catalytically active sites of HWO by Mo framework substitution. The Mo–HWO catalyst showed high activity in SCR, even in the presence of high-concentration $SO_2$ (2700 mg $m^{-3}$) and 10 vol% $H_2O$. The SXRD, TEM, $^1H$ MAS NMR, and $H_2$-TPR data demonstrated that the tunnel openings on the (001) top-facets of the Mo–HWO rods are the catalytically active sites, *i.e.*, they consist of hexagonal hollow sites surrounded by six $WO_6$ and $MoO_6$ octahedra. XANES and XPS data in conjunction with DFT calculations exhibited that the Mo framework substitution reduces the bandgap between the HOMO and LUMO, leading to the co-existence of multivalent W and Mo cations in Mo–HWO by hybridizing W and Mo with the bridging oxygen ions of W–O–Mo. The decrease in bandgap and the co-existence of multivalent metal cations may make the electrons produced from the SCR redox cycles transfer between the reactants and the CASs more easily, thus enhancing the activity.

## Acknowledgements

This work was financially supported by the NSFC (21477023) and the STCSM (14JC1400400). The SXRD measurements were conducted at the SSRF.

## Notes and references

1 B. J. Finlayson-Pitts and J. N. Pitts Jr., *Atmospheric chemistry: Fundamentals and experimental techniques*, John Wiley and Sons, New York, U.S.A., 1986.

 This journal is © The Royal Society of Chemistry 2017

Published on 25 April 2017. Downloaded by Fudan University on 11/28/2018 6:17:42 AM.

2 G. Busca, L. Lietti, G. Ramis and F. Berti, *Appl. Catal., B*, 1998, **18**, 1–36.
3 P. Granger and V. I. Parvulescu, *Chem. Rev.*, 2011, **111**, 3155–3207.
4 L. Lietti, I. Nova, G. Ramis, L. Dall'Acqua, G. Busca, E. Giamello, P. Forzatti and F. Bregani, *J. Catal.*, 1999, **187**, 419–435.
5 F. J. J. G. Janssen, F. M. G. Van den Kerkhof, H. Bosch and J. R. Ross, *J. Phys. Chem.*, 1987, **91**, 5921–5927.
6 F. J. J. G. Janssen, F. M. G. Van den Kerkhof, H. Bosch and J. R. Ross, *J. Phys. Chem.*, 1987, **91**, 6633–6638.
7 F. Kapteijn, L. Singoredjo and A. Andreini, *Appl. Catal., B*, 1994, **3**, 173–189.
8 L. Singoredjo, R. Korver, F. Kapteijn and J. Moulijn, *Appl. Catal., B*, 1992, **1**, 297–316.
9 J. Li, H. Chang, L. Ma, J. Hao and R. T. Yang, *Catal. Today*, 2011, **175**, 147–156.
10 V. I. Marshneva, E. M. Slavinskaya, O. V. Kalinkina, G. V. Odegova, E. M. Moroz, G. V. Lavrova and A. N. Salanov, *J. Catal.*, 1995, **155**, 171–183.
11 H. Matralis, S. Theret, Ph. Bastians, M. Ruwet and P. Grange, *Appl. Catal., B*, 1995, **5**, 271–281.
12 G. Ramis, G. Busca, C. Cristiani, L. Lietti, P. Forzatti and F. Bregani, *Langmuir*, 1992, **8**, 1744–1749.
13 J. M. G. Amores and V. S. Escribano, *J. Mater. Chem.*, 1995, **5**, 1245–1249.
14 M. Kobayashi and K. Miyoshi, *Appl. Catal., B*, 2007, **72**, 253–261.
15 L. Dall'Acqua, I. Nova, L. Lietti, G. Ramis, G. Busca and E. Giamello, *Phys. Chem. Chem. Phys.*, 2000, **2**, 4991–4998.
16 Z. Huang, H. Li, J. Gao, X. Gu, L. Zheng, P. Hu, Y. Xin, J. Chen, Y. Chen, Z. Zhang, J. Chen and X. Tang, *Environ. Sci. Technol.*, 2015, **49**, 14460–14465.
17 M. M. Natile, F. Tomaello and A. Glisenti, *Chem. Mater.*, 2006, **18**, 3270–3280.
18 C. Genin, A. Driouiche, B. Gérand and M. Figlarz, *Solid State Ionics*, 1992, **53–56**, 315–323.
19 B. Xue, J. Peng, Z. Xin, Y. Kong, L. Li and B. Li, *J. Mater. Chem.*, 2005, **15**, 4793–4798.
20 C. S. Griffith and V. Luca, *Chem. Mater.*, 2004, **16**, 4992–4999.
21 O. Merdrignac-Conanec and P. T. Moseley, *J. Mater. Chem.*, 2002, **12**, 1779–1781.
22 Y. Zhou, K. Zheng, J. Grunwaldt, T. Fox, L. Gu, X. Mo, G. Chen and G. R. Patzke, *J. Phys. Chem. C*, 2011, **115**, 1134–1142.
23 R. Zhu, *Inorganic Chemistry*, Advanced Education Press, Beijing, 2003.
24 A. V. Karakurkchi, N. D. Sakhnenko and I. Y. Yermolenko, *Russ. J. Appl. Chem.*, 2015, **88**, 1860–1869.
25 O. S. Owen and H. H. Kung, *J. Mol. Catal.*, 1993, **79**, 265–284.
26 G. Kresse and J. Furthmüller, *Phys. Rev. B: Condens. Matter Mater. Phys.*, 1996, **54**, 11169–11186.
27 G. Kresse and J. Furthmüller, *Comput. Mater. Sci.*, 1996, **6**, 15–50.
28 J. P. Perdew, J. A. Chevary, S. H. Vosko, K. A. Jackson, M. R. Pederson, D. J. Singh and C. Fiolhais, *Phys. Rev. B: Condens. Matter Mater. Phys.*, 1992, **46**, 6671–6687.
29 J. P. Perdew, K. Burke and M. Ernzerhof, *Phys. Rev. Lett.*, 1996, **77**, 3865–3868.
30 I. M. Szilágyi, B. Fórizs, O. Rosseler, Á. Szegedi, P. Németh, P. Király, G. Tárkányi, B. Vajna, K. Varga-Josepovits, K. László, A. L. Tóth, P. Baranyai and M. Leskelä, *J. Catal.*, 2012, **294**, 119–127.
31 E. García-González, M. D. Soriano, E. Urones-Garrote and J. L. Nieto, *Dalton Trans.*, 2014, **43**, 14644–14652.
32 C. Yue, X. Zhu, M. Rigutto and E. Hensen, *Appl. Catal., B*, 2015, **163**, 370–381.
33 R. D. Shanon, *Acta Crystallogr., Sect. A: Cryst. Phys., Diffr., Theor. Gen. Crystallogr.*, 1976, **32**, 751–767.
34 T. Wang, Y. Li, J. Li, Z. Feng, D. Sun, B. Zhao, Y. Xu, R. Li and H. Cai, *RSC Adv.*, 2014, **4**, 43366–43370.
35 A. Phuruangrat, D. J. Ham, S. J. Hong, S. Thongtem and J. S. Lee, *J. Mater. Chem.*, 2010, **20**, 1683–1690.
36 L. Chen, S. Lam, Q. Zeng, R. Amal and A. Yu, *J. Phys. Chem. C*, 2012, **116**, 11722–11727.
37 S. Salmaoui, F. Sediri, N. Gharbi, C. Perruchot, S. Aeiyach, I. A. Rutkowska, P. J. Kulesza and M. Jouini, *Appl. Surf. Sci.*, 2011, **257**, 8223–8229.
38 L. Zheng, M. Zhou, Z. Huang, Y. Chen, J. Gao, Z. Ma, J. Chen and X. Tang, *Environ. Sci. Technol.*, 2016, **50**, 11951–11956.
39 I. M. Szilágyi, J. Madarász, G. Pokol, P. Király, G. Tárkányi, S. Saukko, J. Mizsei, A. L. Tóth, A. Szabó and K. Varga-Josepovits, *Chem. Mater.*, 2008, **20**, 4116–4125.
40 H.-J. Lunk, M. Salmen and D. Heidemann, *Int. J. Refract. Met. Hard Mater.*, 1998, **16**, 23–30.
41 R. C. Slade, P. R. Hirst and B. C. West, *J. Mater. Chem.*, 1991, **1**, 281–288.
42 C. Yue, X. Zhu, M. Rigutto and E. Hensen, *Appl. Catal., B*, 2015, **163**, 370–381.
43 C. Bigey, L. Hilaire and G. Maire, *J. Catal.*, 1999, **184**, 406–420.
44 P. Hu, Z. Huang, Z. Amghouz, M. Makkee, F. Xu, F. Kapteijn, A. Dikhtiarenko, Y. Chen, X. Gu and X. Tang, *Angew. Chem., Int. Ed.*, 2014, **53**, 3418–3421.
45 G. Poirier, M. Nalin, Y. Messaddeq and S. J. L. Ribeiro, *Solid State Ionics*, 2007, **178**, 871–875.
46 O. S. Owen and H. H. Kung, *J. Mol. Catal.*, 1993, **79**, 265–284.
47 G. N. Vayssilov, Y. Lykhach, A. Migani, T. Staudt, G. P. Petrova, N. Tsud, T. Skála, A. Bruix, F. Illas, K. C. Prince, V. Matolín, K. M. Neyman and J. Libuda, *Nat. Mater.*, 2011, **10**, 310–315.